ChemElectroChem

Research Article
doi.org/10.1002/celc.202300185

Chemistry
Europe
European Chemical
Societies Publishing

www.chemelectrochem.org

Ex situ/Operando X-Ray Absorption Spectroscopy on $Fe_{0.07}Zr_{0.93}O_{2-\delta}$/C vs. Fe—N—C as Pt-Group-Metal-Free Oxygen Reduction Reaction Catalysts in Proton Exchange Membrane Fuel Cells

Ana Marija Damjanović,[a] Anna Theresa Sophie Freiberg,[a] Armin Siebel,[a] Burak Koyutürk,[a] Davide Menga,[a] Kevin Krempl,[a] Pankaj Madkikar,[a] Olivier Proux,[b] Hubert Andreas Gasteiger,[a] and Michele Piana*[a]

In this study, ex situ and operando X-ray absorption spectroscopy (XAS) is employed to shed light on structure and degradation mechanism of Fe-based catalysts for the oxygen reduction reaction (ORR) in proton exchange membrane fuel cells (PEMFCs). Ex situ XAS on pristine $Fe_{0.07}Zr_{0.93}O_{2-\delta}$/C catalyst confirms the incorporation of Fe^{3+} in the ZrO_2 structure and clearly exclude any significant presence of Fe—N—C-type structures. The edge shift in data on in-house aged samples demonstrates a mixed oxidation state of Fe (Fe^{3+} and Fe^{2+}), consistent with Fe demetalation from the ZrO_2 structure. Furthermore, a more symmetric coordination in the pre-edge shape points towards the formation of oxidic Fe clusters upon aging. Fe demetalation is inferred also from the edge shift to higher energy (presence of Fe^{3+}) in operando XAS data at 0.3 V, due to Fe phases not electrically polarizable/reducible at the applied voltage. Electrochemical data exclude any correlation between extent of aging and type of test, also for a commercial Fe—N—C catalyst by Pajarito Powder. The observed faster aging for $Fe_{0.07}Zr_{0.93}O_{2-\delta}$ compared to Fe—N—C is attributed to an improved mass transport to/from active sites, manifest also in very similar initial current densities at 0.3 V, despite much higher catalyst activity for Fe—N—C.

Introduction

Proton exchange membrane fuel cells (PEMFCs) are considered electric-vehicle powertrains that can drastically reduce pollution and the carbon footprint of the transport sector, if fueled by hydrogen from renewable energy sources, with the final aim to mitigate the global climate change.[1,2] In the last years, after extended research efforts, several automotive companies commenced the commercialization of fuel cell electric vehicles (FCEVs). Still, the capital and operating costs of FCEVs are significantly higher compared to battery electric vehicles (BEVs).[3] Thompson et al.[4] projected stack costs for light-duty vehicles at a production volume of 0.5 million units/year and concluded that the cost of the platinum-based catalysts would amount to 41% of the total costs. This large fraction can be significantly reduced using platinum-group-metal (PGM)-free catalysts on the cathode, where most of the platinum is needed because of the kinetically sluggish oxygen reduction reaction (ORR).[5] In the last decade, studies about PGM-free ORR catalysts focused on Fe-based catalysts, mainly on the so-called Fe—N—C catalysts[6] whose performance in the kinetic region of the ORR (i. e., at low overpotentials) has come close to that of carbon-supported Pt nanoparticles.[7]

Unfortunately, rapid degradation upon operation is the next important challenge to overcome for Fe—N—C catalysts, as reviewed in some articles throughout the last years.[8–12] A recoverable activity decay, under conditions where no ORR occurs, was originally reported and attributed to polymeric anions reversibly binding to the N-groups that are protonated at pH of 1 and below.[13,9] Already for the first synthesized Fe—N—C catalysts, it was evident, during active-site stability tests using the rotating ring-disk electrode (RRDE) method, how H_2O_2 could strongly contribute to the decomposition of catalytic sites.[14,15] Therefore, the gradual performance degradation in PEMFCs was interpreted as a result of the chemical attack on catalytic sites by H_2O_2 produced during ORR.[14] Later on, H_2O_2 generation during PEMFC tests was again hypothesized as origin of the long-term performance degradation together with the low graphitic character of the carbon support matrix.[16] Voltage cycling tests to high cathode potentials in an RDE configuration (between 20 °C and 80 °C) showed a simultaneous

[a] A. M. Damjanović, A. T. S. Freiberg, Dr. A. Siebel, Dr. B. Koyutürk, Dr. D. Menga, K. Krempl, Dr. P. Madkikar, Prof. Dr. H. A. Gasteiger, Dr. M. Piana
Technical University of Munich
TUM School of Natural Sciences
Department of Chemistry and Catalysis Research Center
Chair of Technical Electrochemistry,
D-85748 Garching (Germany)
E-mail: michele.piana@tum.de
[b] Dr. O. Proux
Observatoire des Sciences de l'Univers de Grenoble (OSUG)
UAR 832 CNRS
Univ. Grenoble Alpes, IRD, INRAe, Météo-France
38041 Grenoble (France)

ChemElectroChem

Research Article
doi.org/10.1002/celc.202300185

Chemistry Europe
European Chemical
Societies Publishing

degradation of active sites and N-doped carbon, strongly increased at elevated temperature, and attributed to carbon corrosion as first step leading to both the dissolution of FeN_x-based active sites and a collapse of the electrode structure.[17,18] The electrochemical oxidation of the carbon surface in an operating PEMFCs, thereby changing its surface properties from hydrophobic to hydrophilic, was also proposed to cause micropore flooding and to be the origin of the initially rather rapid fuel cell performance decay.[19] This hypothesis was readily criticized after examining the double layer capacitance in PEMFCs, reporting that the wetting of micropores already occurred prior to any stability tests and that the small changes in the double layer capacitance following a degradation test were too small to relate to the observed strong performance degradation.[20] Carbon oxidation by H_2O_2 as primary origin of the performance decay was further postulated afterwards, still without excluding active-site protonation/anion binding and micropore flooding as side mechanisms, but, on the contrary, discarding demetalation.[21] Another article also postulated the same origin of degradation of the carbon support adjacent to the active sites in H_2O_2 acidic environment, and related this to a mechanism of weaker O_2 binding on Fe-based sites, which are left untouched.[22] On the contrary, demetalation was reported more recently as origin of the initial loss of ORR activity, hypothesizing the dissolution of Fe in the water phase that is filling the micropores.[23] An Fe–N–C catalyst, synthesized in a way as to avoid impurities of metallic Fe phases and containing only atomically dispersed Fe active sites, was degraded via an RDE-based potential-cycling accelerated stress tests, confirming Fe cleavage from the active site, even with formation of Fe clusters, as well as carbon corrosion as causes of degradation.[24] A further confirmation of the same origin of the activity loss using similar tests was reported,[25,26] ascribing the effect to H_2O_2 and reactive oxygen radical species produced by a Fenton's reaction on the Fe sites obtained after demetalation. A comparison between Co–N–C and Fe–N–C catalysts reported carbon oxidation combined with a demetalation mechanism, with a weaker effect in the case of the Co-based catalyst, presumably due to its lower activity for the Fenton's reaction.[27]

X-ray absorption spectroscopy (XAS) at the Fe K-edge revealed to be an essential characterization technique to probe Fe–N–C catalytic moieties. Oxidation state and coordination geometry can be inferred using X-ray absorption near-edge structure (XANES), while coordination numbers, bond distances, and local order can be inferred from extended X-ray absorption fine structure (EXAFS). Ex situ XAS analyses on Fe–N–C catalysts allowed for the structural characterization of various Fe sites and their correlation to different ORR activities, aiming at an improved synthesis towards an optimized ORR performance.[28,29] In situ measurements are fundamental for identification of electronic and structural properties in real active sites, i.e., during actual ORR conditions.[30]

The first reproduced and evident correlation between in situ XAS data and electrochemical parameters was the monotonous shift of both XANES and EXAFS features upon potential polarization of Fe–N–C electrodes.[31–35] This behavior was attributed to the adsorption-desorption step $(H)O-Fe^{3+}-N_4 \rightleftarrows Fe^{2+}-N_4,$[30]

chemically depicting water activation forming Fe^{3+} at high potentials, gradually shifted to oxygen-uncoordinated Fe^{2+} at low potentials, which is considered the real ORR active site. This activation/deactivation mechanism is the origin of the long-known direct correlation between ORR-polarization onset potentials and Fe^{3+}/Fe^{2+} redox intrinsic potentials, characteristic of each Fe–N–C catalyst.[31–34,36] This mechanism allowed the theorization of the dynamic site-blocking effect, related to $-O(H)$ coverage (blocking) of Fe^{2+} active sites and governed by the relation between cathode operating potential and Fe^{3+}/Fe^{2+} catalyst intrinsic redox potential.[33,37,38] The consequences of this effect are that ORR currents are limited at high potentials purely by specific catalytic activity, while at low potentials they are limited either by site blocking and/or by specific activity, depending on the Fe^{3+}/Fe^{2+} intrinsic redox potential.

Comparing in situ and ex situ data,[33] it was evident that ex situ Fe–N–C moieties (in contact with air) are comparable to in situ oxygen-coordinated Fe^{3+} sites at high potentials,[31] and have been confused with the uncoordinated real active sites. A combination of XANES and EXAFS analyses contributed further to structural understanding of the most active sites and their behavior upon oxygen adsorption in comparison to Fe phthalocyanine.[33,37] While oxygen-uncoordinated Fe phthalocyanine showed the typical square-planar $Fe^{2+}-N_4$ structure (D_{4h} symmetry) - where Fe^{2+} is brought out of plane upon oxygen coordination - oxygen-uncoordinated Fe^{2+} is located off the $Fe^{2+}-N_4$ plane and moves back to the planar configuration upon oxygen adsorption on the most active pyrolyzed catalysts.[33,37] Density functional theory (DFT) calculations[33] suggested that the off-plane oxygen-uncoordinated configuration suppresses Fe-to-N electron back-donation, increasing the d-electron density on Fe, thus allowing an easier coordination to oxygen and a higher redox intrinsic potential. Furthermore, the in-plane oxygen-coordinated Fe^{3+} weakens the Fe–O bond, thereby improving the ORR activity. XANES fingerprints of different Fe species can support the speciation of inactive sites after degradation of Fe-based catalysts with the help of complementary analytical techniques.[39]

While many studies are available on in situ XAS characterization of Fe–N–C catalysts and their degradation in PEMFCs, such studies are still missing for the PGM-free catalyst $Fe_{0.07}Zr_{0.93}O_{2-\delta}/C$, whose synthesis and characterization we had reported in our publication.[40] In this previous article, we shed light on the structure of our as-synthesized catalyst using soft X-ray techniques and Mössbauer spectroscopy, demonstrating that it consists of Fe^{3+} ions in high-spin state, which substitute Zr^{4+} ions in nanometric tetragonal ZrO_2. DFT calculations suggested that the substitution of aliovalent cations in the structure would enhance the formation of oxygen vacancies, being the likely reason for the increased specific ORR activity vs. pure nanometric tetragonal ZrO_2. ZrO_2 was studied as PGM-free ORR catalyst in one of our previous publications for its potential stability in the strongly acid PEMFC environment but showing need of strong improvements in ORR activity.[41]

In this work, first, we report ex situ XAS data to obtain confirmation and further structural information about pristine and aged $Fe_{0.07}Zr_{0.93}O_{2-\delta}/C$ ORR catalysts. Furthermore, using

ChemElectroChem

Research Article
doi.org/10.1002/celc.202300185

**Chemistry
Europe**
European Chemical
Societies Publishing

operando XAS we strengthen the conclusions drawn from ex situ data, aiming at understanding which degradation mechanism rules the performance losses experienced during PEMFC operation of in-house synthesized PGM-free catalyst, and at finding any possible correlation between catalyst degradation and the specific PEMFC operating conditions. We also compare XAS and electrochemical data on $Fe_{0.07}Zr_{0.93}O_{2-\delta}/C$ to similar data collected using a commercial Fe—N—C catalyst provided by Pajarito Powder, discussing possible discrepancies between them.

Results and Discussion

Ex situ XAS on Pristine and Aged Samples

$Fe_{0.07}/Zr_{0.93}O_{2-\delta}/C$ catalyst (Fe K−edge). Ex situ XANES spectra at the Fe K-edge for pristine and aged gas diffusion electrodes (GDEs) prepared with the in-house synthesized $Fe_{0.07}Zr_{0.93}O_{2-\delta}/C$ catalyst are reported in Figure 11 > a in comparison to FeO,[42] Fe_3O_4, Fe_2O_3 and Fe—N—C (digitalized from literature data[33]) reference materials. The pristine GDE (dark blue line) shows an edge position at the highest energy (comparable to Fe_2O_3, red line) and an intense so-called white line. Both observations are conclusive for a very prominent oxidic environment around a scattering Fe^{3+} ion, likely characterized by better defined energy levels in the density of states than standard oxide samples, inferred by the intense dipole-allowed $1s{\rightarrow}4p$ transition (white line) and consistent with a metal substitution in an insulating ZrO_2 matrix. The difference between fingerprint XANES features of the GDE with the pristine $Fe_{0.07}Zr_{0.93}O_{2-\delta}/C$ catalyst and Fe_2O_3 confirms once again that Fe is not segregated from the ZrO_2 structure.[43] The comparison with

XANES data of a pure Fe—N—C catalyst digitalized from literature data[33] (blue line) shows once more the completely different Fe oxidation state and coordination of the $Fe_{0.07}Zr_{0.93}O_{2-\delta}/C$ catalyst in the pristine GDE, clearly excluding a significant presence of Fe—N—C moieties for the in-house synthesized $Fe_{0.07}Zr_{0.93}O_{2-\delta}/C$ catalyst, as already concluded in our previous publication.[40]

Further information about the redox state of Fe can be obtained by analysis of the pre-edge of XANES data, related to the $1s{\rightarrow}3d$ (quadrupolar) electronic transition.[44] A shift towards higher energies also reflects an increased Fe oxidation state. The pre-edge data of pristine GDE with the $Fe_{0.07}Zr_{0.93}O_{2-\delta}/C$ catalyst (Figure 1 b) confirm a high-energy position due to Fe at high oxidation state (similar to Fe_2O_3, red line), clearly shifted in comparison to that of the Fe—N—C catalyst (blue line, very similar to FeO, dark yellow), and a low peak intensity due to asymmetric/disordered Fe coordination with neighboring atoms. From both portions of XANES data we can confidently conclude once more that our catalyst consists of Fe ions inside the structure of ZrO_2 nanoparticles and that no Fe—N—C moieties are present.

From the in-house-conducted testing protocol for ex situ XAS data collection, (see the paragraph *"Single-cell PEMFC Test Conditions and Protocols"* in the experimental section) XANES data at the Fe K-edge (Figure 1 a) of aged GDE with the $Fe_{0.07}Zr_{0.93}O_{2-\delta}/C$ catalyst (dark cyan line) show a drastic shift of the edge position to lower energy (comparable to Fe_3O_4, green line) and a decreased white-line intensity. These observations are respectively consistent with lower and mixed (Fe^{2+} and Fe^{3+}) Fe oxidation states and less defined electronic energy levels (i.e., at least a decreased amount of Fe in the ZrO_2 structure). The pre-edge data shown in Figure 1 b confirm a shift of the peak onset to lower energy due to the appearance of a shoulder and show a more intense peak due to more
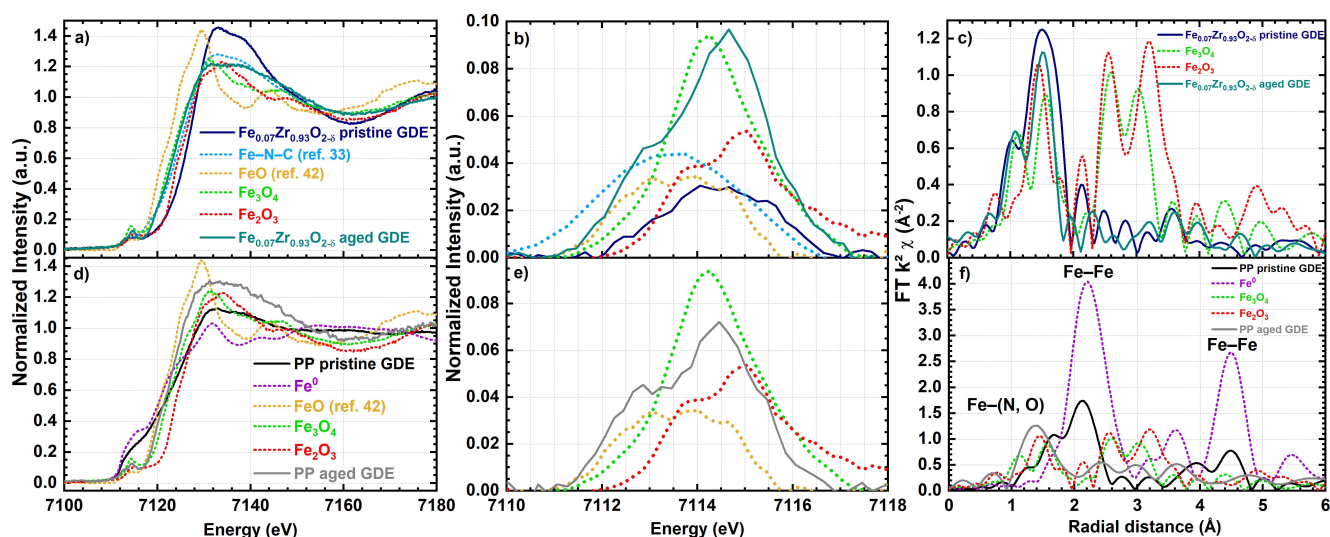

Figure 1. a) XAS spectra at the Fe K-edge in the XANES region of pristine (dark blue) and aged (dark cyan) GDEs with the $Fe_{0.07}Zr_{0.93}O_{2-\delta}/C$ catalyst compared to the standard reference samples: FeO,[42] Fe_3O_4, Fe_2O_3, and Fe—N—C (digitalized from Ref. [33]). b) Pre-edge after background subtraction of normalized XANES spectra in a). c) k^2-weighed Fourier transform of EXAFS spectra from electrodes and standard samples in a), not corrected for phase shift. d) XAS spectra at the Fe K-edge in the XANES region of pristine (black) and aged (gray) GDEs with the Pajarito Powder (PP) catalyst compared with reference materials Fe^0, FeO,[42] Fe_3O_4, and Fe_2O_3. e) Pre-edge after background subtraction of the XANES normalized spectra in d) (the pre-edge of the pristine GDE with the PP catalyst is not shown because of masking by Fe^0). f) k^2-weighed Fourier transform of EXAFS spectra from the samples in d), not corrected for phase shift.

ChemElectroChem

Research Article
doi.org/10.1002/celc.202300185

Chemistry Europe
European Chemical
Societies Publishing

symmetric coordination around the Fe ions. All the observations are consistent with Fe ions at lower oxidation state leaving, at least partially, the ZrO_2 structure and forming more ordered, likely oxidic iron clusters. We also considered the possibility of the interaction of Fe ions with the proton-exchange sites in the ionomer, which we evaluated by preparing a Nafion membrane exchanged with Fe ions and collecting XAS data on it. In the XANES data (not shown), the iron pre-edge of such an Fe ion exchanged membrane has very low intensity (expected asymmetric/disordered interaction) and a different edge shape, allowing us to conclude that this cannot be the main final degradation product after disassembly and storage of the electrochemically aged MEA in ambient air.

Fourier transforms of EXAFS data from GDEs and standard reference samples are reported in Figure 1c (the relative full spectra in energy- and k-space are reported in Figure S1a and b). At a first glance, in both pristine and aged GDEs with $Fe_{0.07}Zr_{0.93}O_{2-\delta}$/C catalyst, the presence of peaks at a position < 2 Å is evident and is very similar to that of the iron oxide standards, in agreement with the conclusions from XANES. The absence of peaks at a position > 2 Å evidences a missing outer shell for both pristine and aged GDEs, hinting towards structural disorder. The Fourier transform of the data from the aged GDE looks to have an intensity ratio of the peaks at 1.1 and 1.5 Å more similar to that of the Fe_3O_4 standard compared to that of the pristine GDE with the $Fe_{0.07}Zr_{0.93}O_{2-\delta}$/C catalyst.

Fe–N–C catalyst by Pajarito Powder. Figure 1d shows XAS spectra in the XANES region at the Fe K-edge for pristine and aged GDEs with the Pajarito Powder catalyst and Fe^0, FeO,[42] Fe_3O_4 and Fe_2O_3 standard materials. Comparing XANES fingerprints of the Fe^0 reference (purple line) and the pristine GDE (black line), a similarity is evident in terms of the presence of an edge feature at low energies (7112–7118 eV) and of a broad feature between 7150 and 7170 eV, demonstrating the presence of Fe^0 in large amount. The XANES spectrum of the aged GDE (gray line) shows an obvious disappearance of the above-mentioned features attributed to Fe^0, concomitant with a white-line intensity increase, both indicating an Fe shift to higher oxidation states.

The k^2-weighed Fourier transforms of EXAFS data (see Figure 1f, the relative full spectra in energy- and k-space are reported in Figure S1c and d) show evident peaks at 2.2 and 4.5 Å for the pristine catalyst (black line), confirmed to be related to Fe–Fe nearest and next-nearest neighbors from their comparison with the Fe^0 reference sample (purple line) and with literature data.[29,32,33,37,45,46] Furthermore, a shoulder at < 2 Å can be assigned to Fe–N nearest neighbors (and in much lower extent to Fe–O from oxygen coordination), characteristic of the active sites of Fe–N–C catalysts.[29,30,32,33,37,47,48] The k^2-weighed Fourier transform of EXAFS data from the aged GDE (gray line) shows the disappearance of the Fe–Fe neighbors at 2.2 and 4.5 Å. Furthermore, the presence of a peak at a lower radial distance of 1.4 Å, attributable to Fe–N and/or Fe–O nearest neighbors, becomes more evident as in all the reference samples (apart from metallic Fe). From these considerations, the EXAFS data confirm the strong evidence from the XANES fingerprints in the pristine GDE of a high amount of metallic Fe

and its disappearance in the aged GDE, suggesting Fe^0 leaching upon electrochemical aging.

Regarding the pre-edge analysis (Figure 1e), using Wilke *et al.*[44] as reference to validate our results, a positive shift of 1 eV is evident in our case, simply explained by the different energy calibration of the first inflection point of data from the Fe^0 reference (7112.00 eV from FAME beamline at ESRF compared to 7111.08 eV in Wilke *et al.*).[44]

Taking a closer look to the pre-edge after background subtraction in Figure 1e, the aged GDE shows broad intense features starting at low energy that, comparing them to Fe_2O_3, Fe_3O_4 and FeO reference data, can be assigned to a mixture of Fe^{2+} and Fe^{3+} oxidation states. It is noteworthy that very similar pre-edge features are observed for the aged GDEs of both Pajarito Powder and $Fe_{0.07}Zr_{0.93}O_{2-\delta}$/C catalysts, pointing towards similar final degradation products.

Knowing the strong variation between XANES fingerprints for Fe^0 and for oxidized Fe phases, a linear combination fitting (LCF) of the XANES data has been attempted to roughly understand the weight fraction of Fe^0 over the total Fe present in the pristine GDE with Pajarito Powder catalyst. With this aim, we used the standard Fe^0 data and the aged GDE as components, being aware that the latter surely contains leached phases that could provide a systematic error to the fitting; this yielded an estimate of ≈ 60 wt% of Fe^0. Unfortunately, because of such a high weight fraction of metallic Fe in the pristine catalyst, further insights on the nature of Fe–N–C active sites and on their degradation upon operation are precluded.[45,46]

$Fe_{0.07}$/$Zr_{0.93}O_{2-\delta}$/C catalyst (Zr $K-edge$). Figure 2a and 2b shows, respectively, ex situ XANES spectra at the Zr K-edge and k^2-weighed Fourier transforms of EXAFS data for pristine (dark blue) and aged (dark cyan) GDEs with the $Fe_{0.07}Zr_{0.93}O_{2-\delta}$/C catalyst, in comparison to pure nanometric ZrO_2/C (orange) reported in our previous studies.[41,49,50] XANES and EXAFS data for pristine Fe-substituted and pure ZrO_2/C show similar results, with a minor broadening of the XANES white line for the former (Figure 2a). After Fourier transform of EXAFS data (Figure 2b, the relative full spectra in energy- and k-space are reported in Figure S2a and b), a decrease in the peak at 3.3 Å for the pristine $Fe_{0.07}Zr_{0.93}O_{2-\delta}$/C catalyst compared to the ZrO_2/C reference material further hints towards structural changes due to Fe incorporation in the ZrO_2 structure.[43] The XANES white line broadening is evidently increased in the aged GDE, as a likely result of Fe leached out of ZrO_2, producing a more vacant and disordered structure. This is further confirmed by the complete absence of the peak at 3.3 Å in the Fourier transform of EXAFS data, hint of a very disordered outer shell after aging. In summary, XAS data at the Zr K-edge confirm the conclusions drawn from Fe K-edge data, namely that Fe is progressively leaving the ZrO_2 structure upon aging of the $Fe_{0.07}Zr_{0.93}O_{2-\delta}$/C catalyst.

ChemElectroChem

Research Article
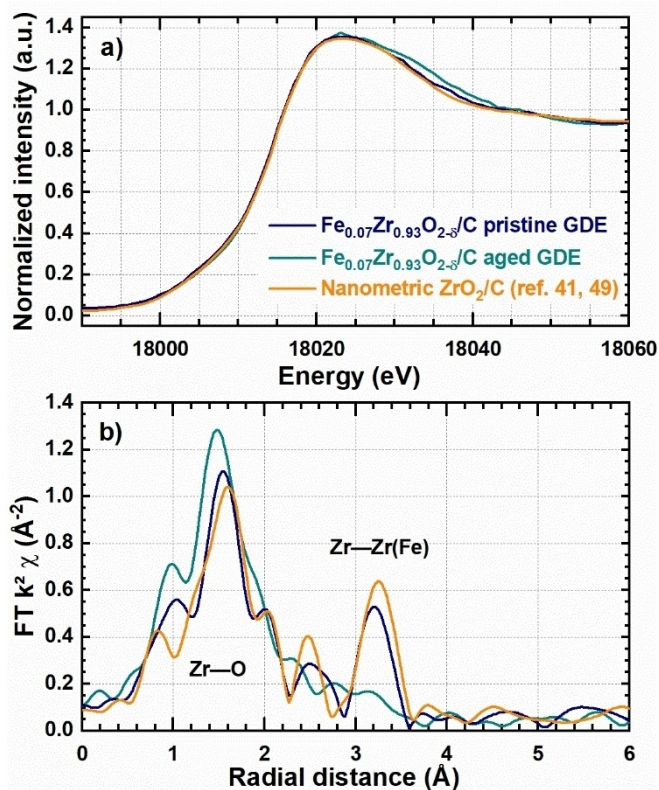doi.org/10.1002/celc.202300185

Chemistry
Europe
European Chemical
Societies Publishing

Figure 2. a) XAS spectra at the Zr K-edge in the XANES region of $Fe_{0.07}Zr_{0.93}O_{2-\delta}$/C pristine (dark blue) and aged (dark cyan) GDEs compared to a powder sample of pure nanometric tetragonal ZrO_2 supported on Ketjenblack carbon (orange), synthesized similarly and reported in previous papers from our group.[41,49] b) k^2-weighed Fourier transform of EXAFS spectra from electrodes and reference sample in a), not corrected for phase shift.

Test in PEMFC and Operando XAS

Validation of operando PEMFC setup. To validate that the H_2/O_2 performance and its degradation obtained using different flow fields and test stations are comparable, three PEMFC tests with the cathode GDEs based on the Fe–N–C catalyst by Pajarito Powder were performed (Figure 3). Linear sweep voltammetry (LSV) measurements in H_2/O_2 before and after a cell potential hold at 0.3 V were collected. Figure 3a shows the results using the in-house graphite flow fields (shown in the inset) and a G60 Greenlight test station, as standard comparison. The graphite flow fields used for operando XAS were tested at both fuel-cell test stations (Figure 3b). Comparing the initial H_2/O_2 LSVs collected with the Greenlight test station, a significant performance difference is observed using flow fields for operando XAS measurements (red line in Figure 3b) vs. standard flow fields (solid green line in Figure 3a). In particular, the current density at 0.7 V is $\approx$2.5 times lower (125 mA cm$^{-2}_{MEA}$ vs. 300 mA cm$^{-2}_{MEA}$) for flow fields used for operando XAS data collection. The reason for this is the higher mass transport limitations at the MEA with operando flow fields, because of the larger and non-optimal channel and land widths, designed to avoid breaking of the locally thinned graphite flow field
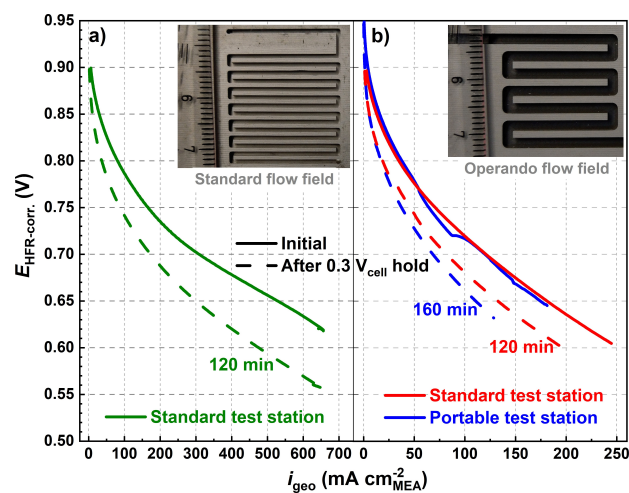

Figure 3. a) Initial H_2/O_2 LSV performance of a GDE with 4.0 mg$_{cat}$ cm$^{-2}_{MEA}$ Pajarito Powder catalyst, measured in-house on a standard Greenlight test station (solid green line) with single-channel/7-serpentines flow field (shown in inset) as well as an LSV after 120 min hold at 0.3 V (dashed green line). b) Initial H_2/O_2 LSV performance of the same GDE type, measured using flow fields designed for operando XAS (shown in inset) either at the standard Greenlight test station (solid red line) or at the portable Fuel Cell Technologies test station for operando measurements (solid blue line). Dashed lines represent H_2/O_2 LSVs after 0.3 V hold for 120 min (red dashed line, standard test station) and 160 min (blue dashed line, portable test station). The segment of LSV curve recorded at the portable test station that deviates from the smooth voltage vs. current curve is related to an unintended deviation in the oxygen pressure. All LSVs were recorded with constant 400 nccm flow of H_2 and O_2 on anode and cathode respectively, at 145 kPa$_{abs}$, 80 °C cell temperature, and 90% RH.

serving as X-ray window, while accommodating channels that are sufficiently wide for the X-ray beam. Additionally, also the high frequency resistance is different for the different flow fields, showing a 2.5-times higher value for the operando flow fields (100 mΩ cm^2 vs. 250 mΩ cm^2). At the same time, Figure 3b shows that the initial LSVs collected at different test stations are basically identical, demonstrating that the two test stations give consistent results. The part of the LSV recorded at the portable test station that is deviating from the smooth decay of voltage vs. current is related to a sporadic deviation of the oxygen pressures (solid blue line in Figure 3b). The cells measured at the different test stations using operando XAS flow fields have different performance after holding at 0.3 V (blue dashed line vs. red dashed line in Figure 3b), likely due to the different operation hold times (120 min vs. 160 min); the hold times were here varied to evaluate the endurance of the cell for the XAS operando measurements. In summary, while different H_2/O_2 performance is observed for different flow-fields, the data suggest that the overall degradation mechanisms do not relate to the flow-field design.

$Fe_{0.07}Zr_{0.93}O_{2-\delta}$/C Catalyst

Electrochemical tests in PEMFCs. Figure 4a to d show details about the various testing protocols conducted with nominally identical cells employing cathode GDEs with $Fe_{0.07}Zr_{0.93}O_{2-\delta}$/C

ChemElectroChem

Research Article
doi.org/10.1002/celc.202300185
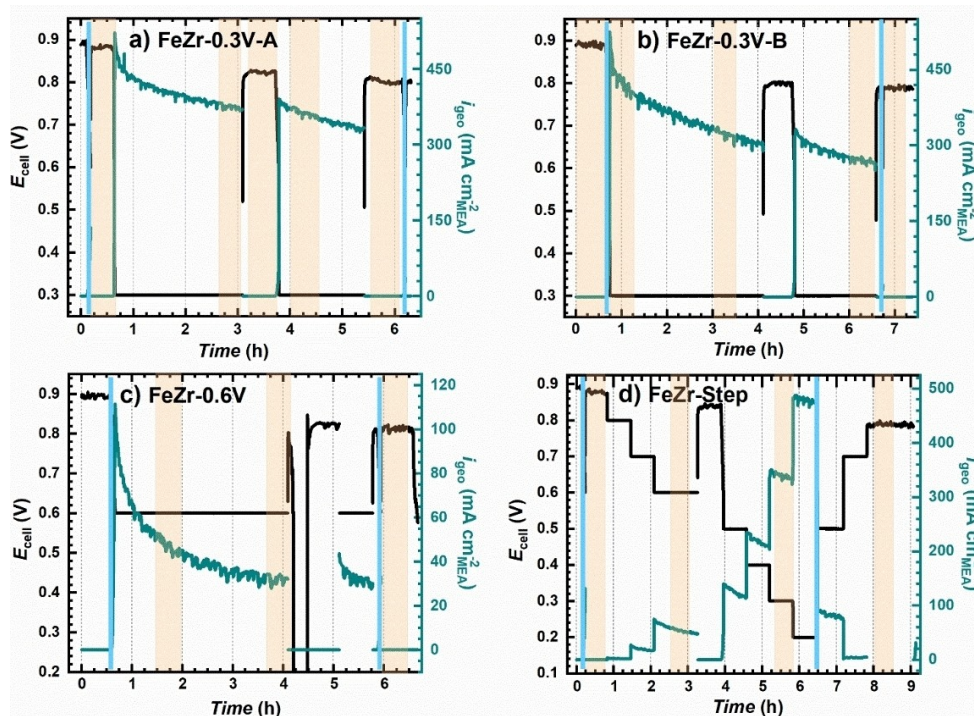
**Chemistry
Europe**
European Chemical
Societies Publishing

Figure 4. Current density (dark cyan) and potential profiles (black) for electrochemical tests conducted with cathode GDEs based on $Fe_{0.07}Zr_{0.93}O_{2-\delta}$/C catalyst, a) and b) during a constant 0.3 V hold under H_2/O_2; c) during a 0.6 V hold under H_2/O_2; d) while varying the cell voltage under H_2/O_2. The vertical light blue lines refer to the periods during which LSVs where recorded, while the orange shadowed regions correspond to operando XAS data collection. All tests and LSVs were recorded with constant 400 nccm flow of H_2 and O_2 on anode and cathode, respectively, at 145 kPa_{abs}, 80 °C cell temperature, and 90 % RH.

(cell voltage in black and current density in dark cyan), all conducted at constant H_2/O_2 flows at the anode/cathode (for more details see paragraph *"Single-cell PEMFC Test Conditions and Protocols"* in the experimental section). Two cells were tested with a constant voltage segment at 0.3 V (shown in Figure 4a and 4b further on referred to "FeZr-0.3V-A" and "FeZr-0.3V-B"), a third cell with a constant voltage segment at 0.6 V (Figure 4c, further on referred to "FeZr-0.6V") and one last cell subjected to a voltage stepping procedure (Figure 4d, further on referred to as "FeZr-Step"). The time periods during which H_2/O_2 LSVs and XAS data were collected are marked by vertical light blue lines and orange shaded regions, respectively. The experiments were designed to monitor both the performance degradation and the change in Fe oxidation state or Zr coordination to neighbors, aiming at correlating XAS to electrochemical performance.

Figure 5a shows LSVs for all the tested cells at the beginning of test (BoT) and the end of test (EoT), while Figure 5b reports the corresponding current densities at BoT (dark-colored bars) and EoT (light-colored bars) acquired at 0.75 and 0.65 $V_{HFR-corr.}$ ($\equiv$ voltage corrected for the high-frequency-resistance) during LSVs, with the numbers inside the bars representing the average current-density decays between BoT and EoT in units of mA cm$^{-2}_{MEA}$ h^{-1}. It is noteworthy that the cells with the highest current densities at the BoT (FeZr-0.3V-A and FeZr-Step) are those tested after a shorter OCV period (see also Figure 4a and 4d), where evidently the catalyst already degrades. The results from these two cells confirm that the LSVs
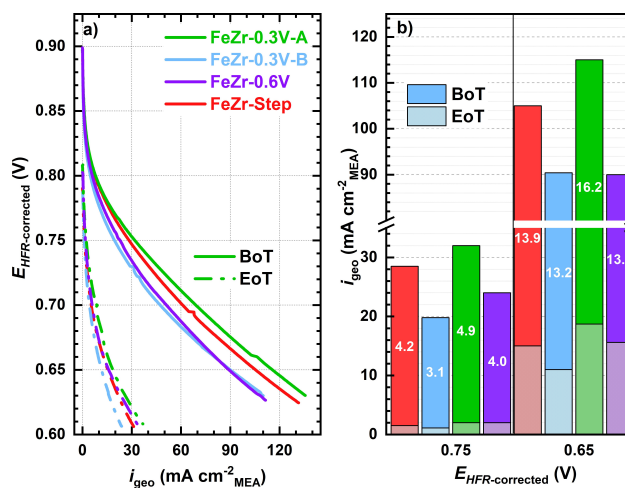

Figure 5. a) LSVs recorded at the beginning of test (BoT, solid lines) and at the end of test (EoT, dash dotted lines) for the four tested cells using cathode GDEs based on the $Fe_{0.07}Zr_{0.93}O_{2-\delta}$/C catalyst. All LSVs were recorded with constant 400 nccm flow of H_2 and O_2 on anode and cathode, respectively, at 145 kPa_{abs}, 80 °C cell temperature and 90 % RH. b) Current densities at 0.75 V and 0.65 $V_{HFR-corr.}$ taken from the LSVs at BoT (darker bars) and EoT (lighter bars); The numbers written inside the bars represent average current-density decays in units of mA cm^{-2} h^{-1} between EoT and BoT.

collected after similar OCV periods show similar results, whereby only very marginal deviations arise from loading differences (maximum ± 10 %), proving data reproducibility. At EoT, all measured cells show similar LSV performances, whereby the

current densities at 0.75 and 0.65 $V_{HFR-corr.}$ are roughly one order of magnitude lower than at BoT. Furthermore, the differences in the current-density decay values (numbers inside the bars of Figure 5b) are only related to the BoT performances (the higher the current density at BoT, the faster the degradation) showing no correlation between catalyst degradation and the different electrochemical testing protocols. The difference in current density decays between 0.75 and 0.65 $V_{HFR-corr.}$ scales, as expected, with the difference in current density between the two voltages.

Operando XAS. During electrochemical tests, operando XAS spectra at Fe and Zr K-edges for the $Fe_{0.07}Zr_{0.93}O_{2-\delta}$/C catalyst were collected over the course of the different testing protocols for each cell (orange shaded areas in Figure 4). The recorded spectra were corrected for pre-edge and post-edge background and normalized for edge intensity. Figure 6a shows XAS operando spectra in the XANES region at the Fe K-edge collected for cell FeZr-0.3V-A (see Figure 4a) that was subjected to a potential hold at 0.3 V. The signal-to-noise ratio of the collected data is relatively low because of both the very low Fe concentration in the sample and the X-ray attenuation in the operando setup. For this reason, the data in the EXAFS region of operando spectra are too noisy and could not be considered.

By comparing the first spectrum recorded at the BoT at OCV (black line) to the pristine GDE with the $Fe_{0.07}Zr_{0.93}O_{2-\delta}$/C catalyst that was collected ex situ (dark blue, same as in Figure 1a) an edge shift to lower energies is already evident after the BoT OCV period. The extent of related partial Fe^{3+} reduction to Fe^{2+} can be estimated by comparing the edge position of the OCV BoT sample to pristine GDE (dark blue, pure Fe^{3+}) and FeO (dark yellow, pure Fe^{2+}), providing a rough 50% of reduction of Fe^{3+} to Fe^{2+}. This effect must be related to a etching/demetalation of Fe^{3+} from the ZrO_2 structure, followed by its transport through the polymer electrolyte to a part of the MEA where H_2 reduces it to Fe^{2+}. The second spectrum was collected after 3 h at 0.3 V (green line) and shows a strong edge shift to a position very similar to FeO (dark yellow).

This is in line with literature observations on Fe—N—C catalysts, where it is attributed to —O(H) desorption (unblocking) and reduction of the Fe sites, which become active.[30] This observation demonstrates that also in our synthesized $Fe_{0.07}Zr_{0.93}O_{2-\delta}$/C catalyst (though very different from Fe—N—C) Fe sites have a very important role in ORR electrocatalysis, as already concluded in our previous papers.[40,50] The spectrum at the second OCV step (red line) shows an edge position very close to the pristine GDE, demonstrating that, at this step, the oxidation state also of the Fe etched from the ZrO_2 structure is mainly Fe^{3+}. Such change of oxidation state in the etched Fe species is evidently related to an increased Fe demetalation and cannot be explained with a Fe redistribution into the cell that would cause an increase of Fe^{2+} concentration in contact to the H_2 side, opposite to the observed trend. The possible reasons for such increase of oxidation state upon Fe demetalation will be discussed in another publication from our group; one hypothesis is related to a neutralization of the acid Nafion ionomer, causing a pH change in the cell, with possible precipitation of Fe^{3+} phases, most likely closer to the cathode,

where Fe ions are etched. A further jump to 0.3 V causes a smaller edge shift to lower energies in the spectrum (light blue line), evidence of the impossibility to polarize part of the Fe, which must be far from the electrode, namely further etched from it. If no demetalation would have happened, the Fe-cations oxidation state would be only related to the applied voltage, without any change upon operation. The spectrum collected at OCV at EoT (dark cyan line) is similar to the previous OCV step, i.e., shows again Fe mainly as Fe^{3+}. In summary, the operando XANES spectra collected at the Fe K-edge further demonstrate the demetalation of Fe and its correlation to catalyst aging.

Figures 6b,c and d show XAS operando spectra in the XANES region at the Zr K-edge collected during the testing protocols with-potential holds at either 0.3 V (see Figure 4b), 0.6 V (see Figure 4c) and during the testing protocol with several potential steps (see Figure 4d). As expected, the changes upon aging are more subtle for Zr ions, but a decreased broadening of the white line appears upon aging with all the testing protocols, hinting toward a more ordered oxygen coordination around Zr. This is opposite to what is reported in the aged sample of Figure 2a and must be related to different aging and storage of the ex situ samples. The little edge shift (≈ 0.5 eV) to higher energy from OCV to the first 0.3 V step in Figure 6b is not significantly larger than the error in the energy scale, thus it is considered meaningless.

Fe—N—C Catalyst by Pajarito Powder

Electrochemical tests in PEMFCs. The details about the electrochemical testing protocols conducted with two nominally identical cells employing cathode GDEs with Pajarito Powder catalyst are shown in Figure 7 (cell voltage in black and current density in light blue) and were all conducted at constant H_2/O_2 flow at the anode/cathode, similarly to the cells with $Fe_{0.07}Zr_{0.93}O_{2-\delta}$/C. The two electrochemical tests consisted of a voltage stepping procedure (PP-Step, Figure 7a, further on referred to "PP-Step") and a constant voltage segment at 0.3 V (Figure 7b, further on referred to "PP-0.3V"). The time periods during which H_2/O_2 LSVs and XAS data were collected are marked by vertical solid orange lines and yellow shaded regions, respectively. The experiments were design to monitor both the performance degradation and the change in Fe^0 content and/or Fe oxidation state. The performance degradation for both PP-0.3V and PP-Step cells after a definite number of hours of operation and at the EoT is evident from the LSVs reported in Figure 8a. The part of the LSV in the PP-0.3V cell that is deviating from the smooth decay in voltage vs. current is caused to a sporadic deviation of the oxygen pressure.

In addition, Figure 8b reports the corresponding geometrical current densities at BoT (filled bars), after 2.8 or 5 h (bars with diagonal stripes) and EoT (bars with vertical stripes) acquired at 0.9 and 0.8 $V_{HFR-corr.}$ during LSVs, with the numbers inside the bars representing the average current-density decays between BoT and 2.8 or 5 h (for PP-Step and PP-0.3V, respectively), and between 2.8 or 5 h and EoT in units of
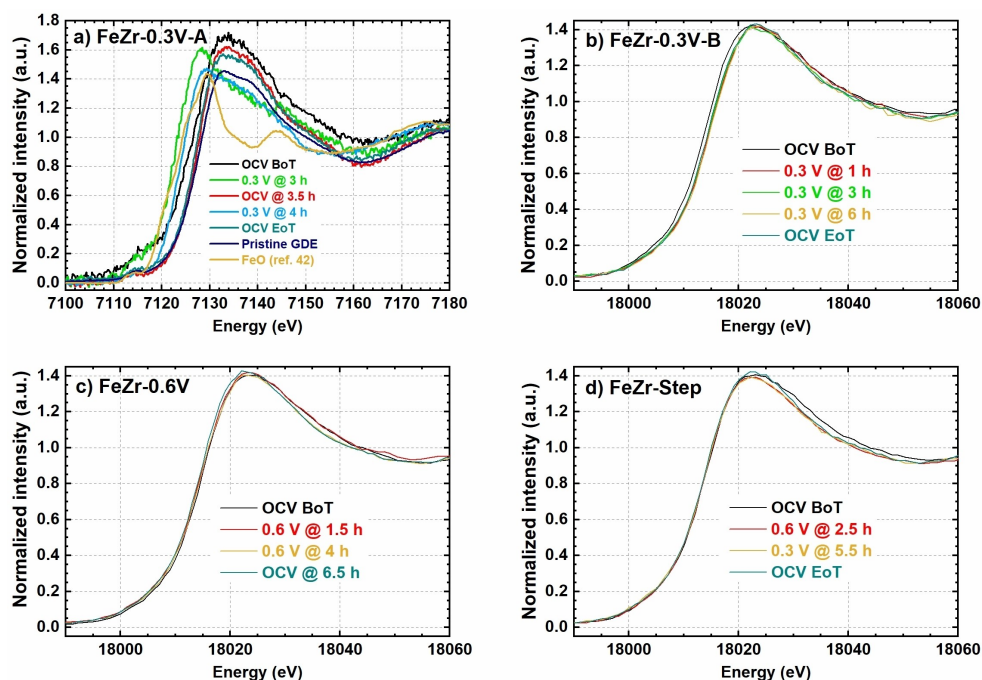
ChemElectroChem

Research Article
doi.org/10.1002/celc.202300185

Chemistry
Europe
European Chemical
Societies Publishing

Figure 6. XAS operando spectra obtained for GDEs based on $Fe_{0.07}Zr_{0.93}O_{2-\delta}$/C catalyst in the XANES region over the course of aging in a PEMFC upon potential hold at 0.3 V: a) at the Fe K-edge (see also Figure 4 a) and b) at the Zr K-edge (see also Figure 4 b). Further data at the Zr K-edge are collected: c) upon potential hold at 0.6 V (see also Figure 4 c) and d) upon potential stepping (see also Figure 4 d). Data from pristine GDEs and FeO[42] are reported for comparison to Fe^{3+}/initial and Fe^{2+}, respectively. The operando spectra are compared with those at OCV at the beginning and end of test.
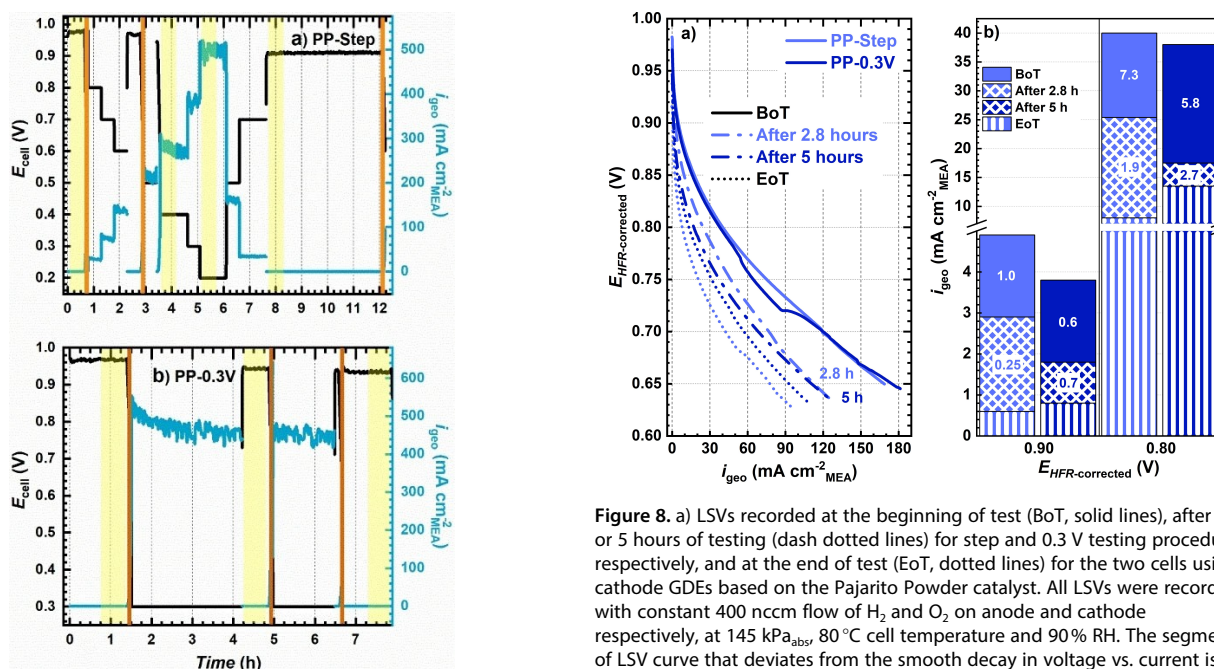

Figure 7. Current density (blue) and potential profiles (black) for electrochemical tests conducted on cathode GDEs with Pajarito Powder catalyst: a) varying the cell voltage and b) during potential hold at 0.3 V, both under H_2/O_2. The vertical brown lines refer to the periods during which LSVs were recorded, while the yellow shadowed regions correspond to operando XAS data collection. All tests and LSVs were recorded with constant 400 nccm flow of H_2 and O_2 on anode and cathode, respectively, at 145 kPa$_{abs}$, 80 °C cell temperature, and 90 % RH.
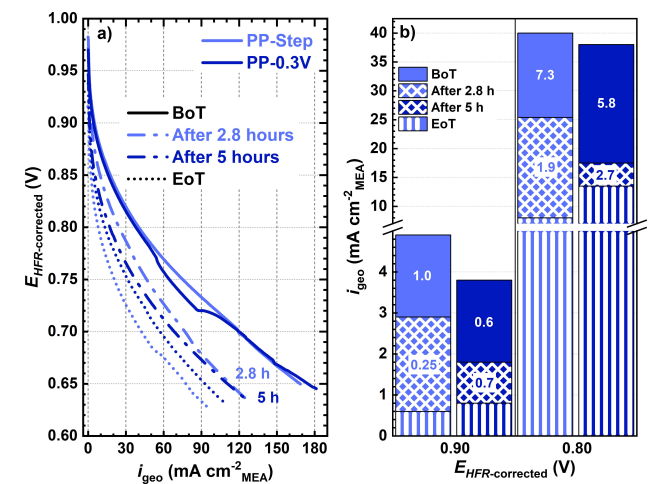

Figure 8. a) LSVs recorded at the beginning of test (BoT, solid lines), after 2.8 or 5 hours of testing (dash dotted lines) for step and 0.3 V testing procedure, respectively, and at the end of test (EoT, dotted lines) for the two cells using cathode GDEs based on the Pajarito Powder catalyst. All LSVs were recorded with constant 400 nccm flow of H_2 and O_2 on anode and cathode respectively, at 145 kPa$_{abs}$, 80 °C cell temperature and 90 % RH. The segment of LSV curve that deviates from the smooth decay in voltage vs. current is related to an unintended deviation in the oxygen pressures. b) Current densities at 0.9 V and 0.8 V$_{HFR-corr.}$ taken from the LSVs at BoT (solid bars), after 2.8 or 5 hours of testing (diagonally-striped bars) and EoT (vertically-striped bars); the numbers marked inside the bars represent the average current-density decays in units of mA cm^{-2} h^{-1} between recorded LSVs.

ChemElectroChem

Research Article
doi.org/10.1002/celc.202300185

**Chemistry
Europe**
European Chemical
Societies Publishing

$mA\,cm^{-2}_{MEA}\,h^{-1}$. The geometrical current densities at 0.9 and 0.8 $V_{HFR\text{-}corr.}$ at BoT (solid lines in Figure 8a and filled bars in Figure 8b) for the two cells show good reproducibility. The PP-Step cell shows a loss in current density of $\approx40\%$ at both 0.9 and 0.8 $V_{HFR\text{-}corr.}$ after 2.8 h of operation (light blue bars with diagonal stripes in Figure 8b), with 0.6 V as last voltage step. The geometrical current densities at the EoT (potential stepping down to 0.2 V and back to OCV, light blue bars with vertical stripes in Figure 8b) shows, in comparison to the BoT, a total significant loss of about 90% and 80% at 0.9 and 0.8 $V_{HFR\text{-}corr.}$, respectively. In the case of the PP-0.3V cell, after 5 h of operation at 0.3 V (dark blue bars with diagonal stripes in Figure 8b), LSVs show a significant loss in current density of $\approx50\%$ for both 0.9 and 0.8 $V_{HFR\text{-}corr.}$. At EoT (after ≈6.5 h), the geometrical-current-density loss at 0.9 and 0.8 $V_{HFR\text{-}corr.}$ further increased to ≈80 and 60%, respectively (dark blue bars with vertical stripes in Figure 8b). Comparing PP-0.3V to PP-Step cell, the former shows lower degradation at EoT, but without experiencing additional 4–5 h of OCV, likely reason for the discrepancy. Furthermore, from the current-density decays reported in Figure 8b, a similar degradation is evident using the two different testing procedures, as reported also for $Fe_{0.07}Zr_{0.93}O_{2-\delta}/C$ cell results, excluding any correlation between catalyst degradation and the different testing procedures. The difference in current-density decays between 0.9 and 0.8 $V_{HFR\text{-}corr.}$ scales, as expected, with the difference in current density between the two voltages. The results also confirm literature reports already showing Fe–N–C catalysts fast degradation usually in the first several hours of operation.[9]

Comparing current-density decays upon operation of cells based on cathode GDEs with Pajarito Powder catalyst (Figure 8b) with those based on $Fe_{0.07}Zr_{0.93}O_{2-\delta}/C$ (Figure 5b), the degradation is significantly faster in the case of the oxide-based carbon-supported catalyst. A likely explanation for this behavior is the remarkable difference in active site accessibility for the two catalysts. $Fe_{0.07}Zr_{0.93}O_{2-\delta}$ is supported on a commercial graphitized Ketjenblack (EA-type carbon), which does not have any microporosity, as reported also in a paper published by our group,[51] thus the active sites are easily accessible via large mesopores, improving mass transport and water management, but also the probability of Fe demetalation and catalyst degradation. On the other hand, in Pajarito Powder catalyst one fifth of pore volume consists of microporosities[52] and, as many other very active Fe–N–C catalysts, it is based on active sites grown in internal micropores formed in situ during catalyst synthesis. Such more difficult accessibility slows down the mass transport of oxygen reduction products away from the active sites,[52] decreasing also the rate of catalyst deactivation. The huge difference in mass transport limitations between the two catalysts is also evident by comparing their average current densities at 0.3 V (Figure 4a and Figure 8b). Despite a much higher catalytic activity for Pajarito Powder catalyst, the average current densities just after applying 0.3 V are both ≈500 $mA\,cm^{-2}_{MEA}$, indicating significant increased mass transport limitations for Pajarito Powder catalyst. In summary, more efficient mass transport and water removal result in higher

access of O_2 to the active site, promoting a better catalyst utilization but also a faster degradation.

Operando XAS. During electrochemical tests, operando XAS spectra at the Fe K-edge for the Pajarito Powder catalyst were collected over the course of the different testing protocols for each cell (yellow shaded areas in Figure 7). The recorded spectra were corrected for pre-edge and post-edge background and normalized for edge intensity. Figure 9a and 9c shows XAS operando spectra at the Fe K-edge in the XANES region collected for the cells PP-Step and PP-0.3V, respectively. In both cases, there is a gradual increment upon operation of the white-line intensity (at ≈7130 eV, red arrow), which is approaching the in-house aged GDE. This trend is evident already by comparing the spectra of pristine GDE and aged GDE from the ex situ analysis (Figure 1d) and it is related to an oxidation of metallic Fe particles over the course of aging. The decreased features at about 7115 eV (blue arrow) and 7160 eV (black arrow), characteristic of Fe^0 fingerprint, confirm this conclusion.

Using a linear combination fitting of the ex situ data from standard Fe^0 and aged GDE (with the assumptions for the aged GDE that metallic Fe is negligible and that the fingerprint of oxidized Fe species is not varying significantly upon aging) we estimated the fraction in wt% of Fe^0 over the total Fe present in the catalyst layer of the pristine sample and over the course of aging. In both PP-Step and PP-0.3V cells, Fe^0 is already decreasing (from the initial LCF-estimated content of 60 wt% in the pristine GDE) after OCV hold before testing protocols to a reproducible 49 and 45 wt% (for PP-Step and PP-0.3V, respectively, see Figure 4a and c), evidencing significant Fe^0 etching in the strongly acidic PEMFC medium. Upon operation, the amount of Fe^0 from LCF decreases down to 36 and 30 wt% after 4 and 4.5 hours of degradation for PP-Step and PP-0.3V, respectively. At the EoT, the presence of Fe^0 decreases to 34 wt% for PP-Step cell (7 h of total test time) and to 18 wt% for PP-0.3V cell (8 h of total test time). The PP-Step cell reaches the minimum amount of metallic Fe after the lowest applied voltage of 0.2 V, showing no further Fe^0 etching despite two subsequent steps at relatively higher potential. On the other hand, the PP-0.3V cell shows a further decrease of Fe^0 to 18 wt% after prolonged 0.3 V constant voltage. Since there is no remarkable difference between the last LSVs of PP-Step and PP-0.3V cells (Figure 8a and b), we can conclude that the Fe^0 etching does not correlate with catalyst degradation, thus likely presume that Fe^0 does not contribute to catalyst ORR activity. The Fourier-transform analysis of EXAFS data in Figure 9b and 9d (the relative full spectra in energy- and k-space are reported in Figure S3a to d) show a gradual decrease of both peaks at 2.2 and 4.5 Å, which can be assigned to the two closest Fe–Fe neighbors in body-centered cubic Fe^0, confirming the decreasing trend for the content of Fe^0 observed in XANES LCF. On the other hand, the intensity of a shoulder at ≈1.5 Å is increasing with time, reaching a defined single peak at ≈1.4 Å in the aged electrode, which is attributable to N or O neighbors in Fe–N–C catalyst and/or in Fe species resulting from its degradation. As already pointed out in literature,[45,46] the significant presence of Fe^0 in the catalyst (see also Figure S4) makes very difficult to

ChemElectroChem

Research Article
doi.org/10.1002/celc.202300185

Chemistry Europe
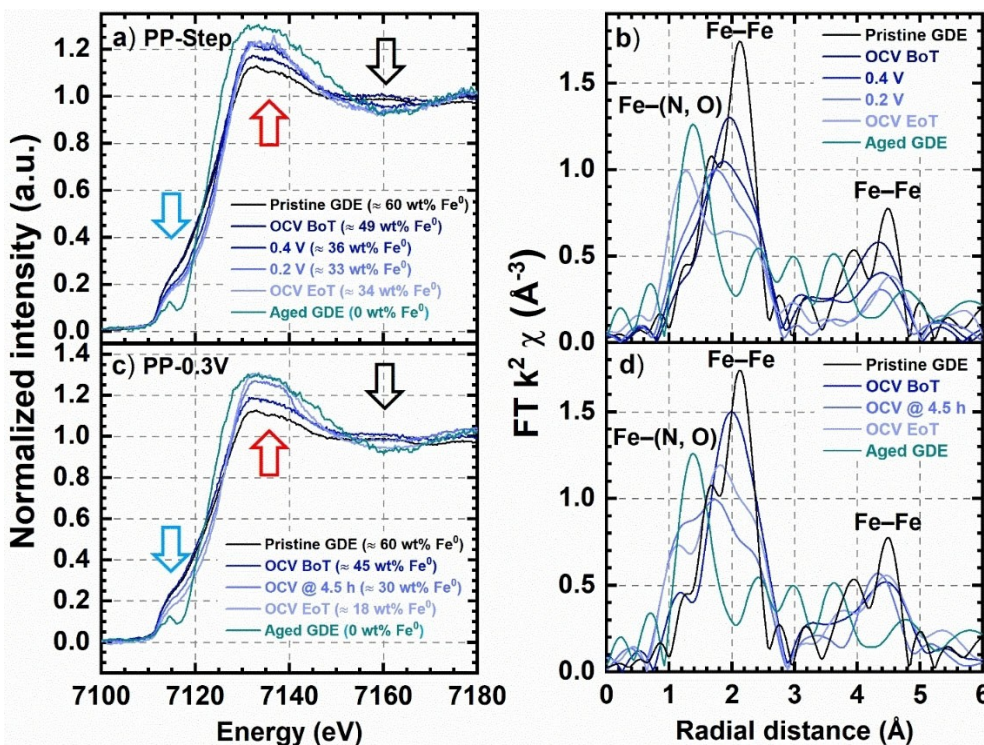European Chemical
Societies Publishing

Figure 9. a) XAS operando spectra at the Fe K-edge in the XANES region obtained in a PEMFC with a cathode GDE using Pajarito Powder catalyst, over the course of aging upon potential stepping (PP-Step, see also Figure 7 a) compared to pristine and aged GDE measured ex situ (see Figure 1 d). b) k^2-weighed Fourier transform of the EXAFS spectra from the cell in a), not corrected for phase shift. c) XAS in situ spectra obtained at OCV in a PEMFC with a cathode GDE using Pajarito Powder catalyst, over the course of aging upon potential hold at 0.3 V (PP-0.3V, see also Figure 7 b) compared to pristine and aged GDE measured ex situ. d) k^2-weighed Fourier transform of EXAFS spectra from the cell in c), not corrected for phase shift.

discriminate during degradation any change in Fe species only attributable to Fe–N–C catalyst or its degradation products.

Conclusion

In conclusion, both pre-edge and fingerprint of XANES ex situ data collected on $Fe_{0.07}Zr_{0.93}O_{2-\delta}$/C confirm the incorporation of Fe^{3+} ions in the ZrO_2 structure and clearly exclude any significant presence of Fe–N–C-type structures. XANES data collected on in-house aged samples demonstrate lower and mixed oxidation state of Fe ions (Fe^{3+} and Fe^{2+}) from the edge shift, and less defined electronic energy levels from the so-called white line, both consistent with the demetalation of Fe from the ZrO_2 structure. Furthermore, a more symmetric coordination in the pre-edge shape points towards the formation upon aging of Fe oxidic clusters. Fe demetalation can be inferred also from the edge shift to higher energy upon aging in operando XANES data at 0.3 V, due to Fe phases not electrical polarizable and reducible by the applied voltage. The electrochemical data exclude any correlation between the extent of aging and the testing protocol, also confirmed for a commercial Fe–N–C catalyst by Pajarito Powder. For the latter, the significant presence of metallic Fe in the pristine sample and its oxidation upon operation as ORR catalyst in a PEMFC is evident from both ex situ and operando XAS data, making it impossible to gain further understanding of Fe–N–C active sites

and of their degradation. The observed faster aging for $Fe_{0.07}Zr_{0.93}O_{2-\delta}$/C vs. Fe–N–C is attributed to an improved mass transport to/from active sites in the former, manifest also in very similar initial current density at 0.3 V, despite much higher catalytic activity for Fe–N–C. This observation demonstrates once more the need of improvement in anchoring and protecting active sites from acid attack and metal etching.

Experimental Section

Synthesis of the $Fe_{0.07}Zr_{0.93}O_{2-\delta}$/C ORR Catalyst

The catalyst was prepared similarly to a previously reported procedure,[40] with the difference in the impregnation step, for which the incipient wetness technique was used to increase the batch size. The pore volume of graphitized Ketjenblack (EA-type carbon, Tanaka Kikinzoku Kogyo K.K., Japan) was titrated with chloroform and the corresponding value was used to dissolve the required amount of metal phthalocyanines. The amount of $ZrCl_2Pc$-(t-Bu)$_4$ (synthesized as reported in our previous publication, similarly to FePc(t-Bu)$_4$)[40] was adjusted to achieve the desired theoretical loading of 12 wt % of ZrO_2. The solution in chloroform of Fe and Zr phthalocyanines in the correct atomic ratio was slowly pipetted onto the graphitized Ketjenblack and the obtained mixture was first sonicated for one hour in an ice-cold ultrasonic bath and then dried in an oven at 80 °C overnight. This powder was then heat treated in a tube furnace (HTM Reetz, Germany) in a quartz boat using the following procedure. First, the tube furnace was purged at room temperature with Ar and subsequently heated

ChemElectroChem

Research Article
doi.org/10.1002/celc.202300185

Chemistry
Europe
European Chemical
Societies Publishing

under flowing 5% H_2 in Ar (1000 nccm) to 1073 K, with a heating rate of 10 K min^{-1} up to 973 K and with 1 K min^{-1} to the final temperature to avoid a temperature overshoot. After holding the final temperature with the same gas flow for 2 h, the gas was switched to partial oxidative treatment with 2.5% H_2 and 0.5% O_2 in Ar (2100 nccm) for another hour. Subsequent cooling occurred naturally under 5% H_2 flow in Ar (1000 nccm).

Membrane Electrode Assembly (MEA) Preparation

The PGM-free catalyst $Fe_{0.07}Zr_{0.93}O_{2-\delta}$/C synthesized in our group (Fe content as metal ≈0.36 wt%$_{cat}$) was compared with a commercially available Fe–N–C catalyst provided by Pajarito Powder (USA, Fe content as metal ≈0.5–1.0 wt%$_{cat}$, batch number: PMF011904). The catalyst inks with either one of the catalysts were prepared by mixing 0.6 g of catalyst powder with 4.3 g 1-propanol at 500 rpm for 5 min in an ARV-310 planetary mixer (Thinky, USA), with 3 mm zirconia beads to cover the bottom of a 12 mL mixing vessel with two layers of beads. Then ≈2 g of a water/propanol dispersion of ionomer (20 wt% of a low equivalent weight EW ≈700, Asahi Kasei, Japan) was added and mixed at the same conditions. The inks were coated onto the microporous layer of a gas diffusion medium H14C10 (Freudenberg, Germany) using a 400 μm gap bar, and dried in an oven at 40 °C. The coating was repeated to get the desired loading, using a 450 μm gap bar, considering the thickness of the first dried layer (≈50 μm). The obtained gas diffusion electrodes (GDEs) were cut out using a cutting tool (Spahn, Germany) to the size of 5 cm^2. The cathode catalyst layers for both catalysts had a loading of 4.0 ± 0.4 mg$_{cat}$ cm$^{-2}_{MEA}$ and an ionomer/carbon (I/C) ratio of 0.65/1. Electrode thicknesses were between 120 and 140 μm for both catalysts, measured by a Mitutoyo dial gauge (accuracy of ±3 μm, series 543). Anode electrodes were prepared using a Pt-based catalyst (TEC10V20E, 20 wt%$_{Pt}$, Tanaka Kikinzoku Kogyo K.K., Japan) and a Pt loading of 0.1 mg$_{Pt}$ cm$^{-2}_{MEA}$. Anode catalyst layers were prepared following the decal-transfer procedure reported in our previous studies.[53,54] MEAs were obtained by first hot-pressing the anode decal onto the membrane (Nafion 212, 50 μm) at 155 °C for 5 min under 4 kN force. Then, the cathode GDEs and the anode-coated membrane were directly assembled in a single-cell PEMFC (see below) without hot pressing.

Single-cell PEMFC Test Conditions and Protocols

All PEMFC measurements were conducted in a 5 cm^2 single cell. In-house measurements were performed on an automated fuel cell test stations (G60, Greenlight Innovations, Canada) using in-house manufactured cell hardware with graphite flow fields (Poco Graphite, USA). The in-house measurements on the automated test stations were carried out using a Reference3000 potentiostat (Gamry, USA), and the electrochemical measurements conducted with the operando set-up were collected with a VSP-300 potentiostat (BioLogic, France). The flow-field design of the in-house tested cells is based on a single channel with 7 serpentines and with 0.8/0.8 mm channel/land width and 0.8 mm channel depth. Operando XAS measurements were performed with a portable, semi-automated fuel cell test station (Fuel Cell Technologies, USA) with special in-house designed and produced cell hardware for this purpose.[55] The graphite flow fields used here have an X-ray graphite window on the cathode side that is thinned to 0.5 mm thickness, so that beam attenuation is limited also in fluorescence mode. Flow fields designed for operando XAS have a single channel with 3 serpentines and 2.0/1.3 mm channel/land width and 1 mm channel depth. The two different flow-field designs are shown in the insets of Figure 3. In both cases, the GDL compression was set to be 20.0 ± 1.0% by adjusting the thickness of PTFE-coated glass-

fiber subgaskets (Fiberflon), assuming 7% compression at the applied force of assembly (torque of 12 N m).

During the electrochemical characterization and operation, the same _testing conditions_ were used for the two different cell setups. The otherwise typically used conditioning of the cell prior to electrochemical characterization was not applied in this study, due to the low electrochemical stability of the PGM-free catalysts.[9] Initially, the cell was heated to 40 °C under H_2/N_2 flows (200/50 nccm, 100%/0% RH) at anode/cathode, followed by cyclic voltammograms (CVs) of the cathode. The CVs were recorded at three different scan rates (50, 100 and 150 mV s^{-1}), and at each scan rate three cycles were collected with nitrogen feed on the cathode (50 nccm, 90% RH) and hydrogen feed on the anode (100 nccm, 90% RH) at 145 kPa$_{abs}$ pressure (inlet controlled). After recording the CVs, an initial linear sweep voltammogram (LSV) from open circuit voltage (OCV) to 0.65 V at a scan rate of 1 mV s^{-1} was recorded under oxygen feed on the cathode (400 nccm) and hydrogen feed on the anode (400 nccm), with 145 kPa$_{abs}$ pressure on both sides, a cell temperature of 80 °C, and temperature of anode and cathode humidifiers set to 78 °C, resulting in 90% relative humidity (RH). Electrochemical impedance spectroscopy (EIS) was recorded before LSV at OCV under hydrogen and oxygen on anode and cathode, respectively, in order to determine the high frequency resistance (HFR) and evaluate the cell ohmic resistance, which was later used for the cell-voltage correction (to get data in V$_{HFR-corr.}$). Gas pressures, relative humidity and cell temperature were kept the same for EIS and LSV measurements. The used EIS frequency range was 1–100 kHz, with 10 points per decade and with 3.5 mV voltage perturbation. This electrochemical-characterization step (LSV and EIS at OCV) was repeated after certain degradation steps, as described in the following paragraph.

Electrochemical tests for ex situ XAS measurements were conducted in-house on both catalysts, using the above-described H_2/O_2 test conditions, 5 cm^2 single-cell hardware, and automated fuel-cell test stations. The cell voltage was consecutively held at OCV, 0.8 V, and 0.3 V for 2 hours each step, collecting a CV, an LSV, and an EIS at OCV before testing and an LSV and EIS at after 2 hours OCV at each operation cycle. The tested MEAs were stored at ambient condition before XAS data collection.

Two different _electrochemical testing protocols_ were used for operando XAS measurements, based on different applied cell potentials, and hold times. The _first testing protocol_ consisted of potential stepping from OCV down to 0.2 V, with 0.1 V step size, and coming then back to OCV through only two voltage steps (0.5 and 0.7 V). The cell was held at each cell potential for at least 30 min, needed for XAS data collection. The _second testing protocol_ consisted of a constant potential hold (at 0.3 V or 0.6 V) for several hours. During the electrochemical tests, the H_2/O_2 operating conditions were kept constant as those described above for the LSVs. LSV and EIS at OCV were recorded after certain time of operation and, at the end of the test, CVs were recorded as described above.

XAS Experimental Details

XAS spectra at Fe and Zr K-edges were collected at the European Synchrotron Radiation Facility (Grenoble, France) on the bending-magnet beamline CRG-FAME (BM30B). The ring was operated at 6 GeV with a nominal current of 90 mA in the 16-bunch mode. The beamline was equipped with a liquid-nitrogen-cooled double-crystal Si(2 2 0) monochromator surrounded by two Rh-coated mirrors for harmonic rejection. For Fe and Zr K-edges, the mirrors were set to 6 mrad and 2.8 mrad to remove harmonics and photons with energy higher than ≈10 keV and ≈21 keV, respectively. The

ChemElectroChem

Research Article
doi.org/10.1002/celc.202300185

**Chemistry
Europe**
European Chemical
Societies Publishing

beam size on the sample was 220×140 μm (H × W, FWHM) The monochromator was energy-calibrated at both Fe and Zr K-edges by setting the first maximum of XAS-spectrum first derivative of metallic Fe and Zr foils to 7112 eV and 17998 eV, respectively. Operando spectra were recorded at the Fe and Zr K-edge in fluorescence mode, at a 45° angle between sample surface and beam, using a CANBERRA 30-element Ge solid-state detector at 90° angle to the beam, while reference and ex situ samples were recorded in transmission mode. XANES-focused Fe K-edge data were collected between 7000 and 7550 eV, with 4 eV step and 2 s per step from 7000 to 7080 eV, then 0.2 eV step and 2 s per step to 7180 eV, while in the EXAFS region a k-step of 0.2 Å^{-1} was used to the ending energy in order to facilitate the background subtraction. More precise operando spectra were collected between 7000 and 7960 eV, with 4 eV step and 2 s per step to 7080 eV, then 0.2 eV step and 2 s per step to 7180 eV, while in the EXAFS region a k-step of 0.05 Å^{-1} was used to the ending energy. The same more precise data collection was performed also on reference and ex situ samples. For the Zr K-edge, detailed data were recorded between 17850 and 18740 eV, with 5 eV step and 2 s per step to 17950 eV, then 1 eV step and 4 s per step to 18000 eV, while in the EXAFS region a k-step of 0.05 Å^{-1} was used to the ending energy.

The beam damage was minimized by switching between several different spots while recording consecutive data. Furthermore, a possible MEA damage was tested by collecting data on the same spot continuously for 3 hours in an operando cell with 1.5 bar$_{gas}$ N$_2$ on the anode and 0.4 bar$_{gas}$ H$_2$ on the cathode, to electrochemically detect any membrane deterioration. No spectroscopic change was detected during this recording time.

XAS data were analyzed using the Demeter software package for normalization and processing of XANES and EXAFS data.[56] The EXAFS was extracted from the raw data and Fourier transform (FT) was obtained from the $k^2 \times \chi(k)$ functions without phase correction. The pre-edge peaks were obtained by background subtraction of a low-degree interpolation function (spline), fitted on data a few eV before and after the pre-edge peaks.[44]

Conflict of Interests

The authors declare no conflict of interests.

Data Availability Statement

The data that support the findings of this study are available from the corresponding author upon reasonable request.

[1] National Renewable Energy Laboratory - US Department of Energy, "The Green Hydrogen Report", can be found under: https://www.hydrogen.energy.gov/pdfs/greenhyd.pdf, **1995** (accessed: April 13, 2023).

[2] European Fuel Cells and Hydrogen Joint Undertaking, "A portfolio of power-trains for Europe: a fact-based analysis", can be found under: https://www.clean-hydrogen.europa.eu/system/files/2014-09/Power_trains_for_Europe_0.pdf, **2010** (accessed: April 13, 2023).

[3] B. G. Pollet, S. S. Kocha, I. Staffell, *Curr. Opin. Electrochem.* **2019**, *16*, 90–95.

[4] S. T. Thompson, B. D. James, J. M. Huya-Kouadio, C. Houchins, D. A. DeSantis, R. Ahluwalia, A. R. Wilson, G. Kleen, D. Papageorgopoulos, *J. Power Sources* **2018**, *399*, 304–313.

[5] S. T. Thompson, D. Papageorgopoulos, *Nat. Catal.* **2019**, *2*, 558–561.

[6] A. A. Gewirth, J. A. Varnell, A. M. DiAscro, *Chem. Rev.* **2018**, *118*, 2313–2339.

[7] M. Lefevre, E. Proietti, F. Jaouen, J. P. Dodelet, *Science* **2009**, *324*, 71–74.

[8] Z. Chen, D. Higgins, A. Yu, L. Zhang, J. Zhang, *Energy Environ. Sci.* **2011**, *4*, 3167–3192.

[9] D. Banham, S. Ye, K. Pei, J. Ozaki, T. Kishimoto, Y. Imashiro, *J. Power Sources* **2015**, *285*, 334–348.

[10] Y. Shao, J. P. Dodelet, G. Wu, P. Zelenay, *Adv. Mater.* **2019**, *31*, e1807615.

[11] X. Wan, X. F. Liu, J. L. Shui, *Prog. Nat. Sci. Mater. Int.* **2020**, *30*, 721–731.

[12] L. Du, V. Prabhakaran, X. Xie, S. Park, Y. Wang, Y. Shao, *Adv. Mater.* **2021**, *33*, e1908232.

[13] J. Herranz, F. Jaouen, M. Lefevre, U. I. Kramm, E. Proietti, J. P. Dodelet, P. Bogdanoff, S. Fiechter, I. Abs-Wurmbach, P. Bertrand, T. M. Arruda, S. Mukerjee, *J. Phys. Chem. C* **2011**, *115*, 16087–16097.

[14] M. Lefevre, J. P. Dodelet, *Electrochim. Acta* **2003**, *48*, 2749–2760.

[15] H. Schulenburg, S. Stankov, V. Schünemann, J. Radnik, I. Dorbandt, S. Fiechter, P. Bogdanoff, H. Tributsch, *J. Phys. Chem. B* **2003**, *107*, 9034–9041.

[16] F. Jaouen, E. Proietti, M. Lefèvre, R. Chenitz, J.-P. Dodelet, G. Wu, H. T. Chung, C. M. Johnston, P. Zelenay, *Energy Environ. Sci.* **2011**, *4*, 114–130.

[17] V. Goellner, C. Baldizzone, A. Schuppert, M. T. Sougrati, K. Mayrhofer, F. Jaouen, *Phys. Chem. Chem. Phys.* **2014**, *16*, 18454–18462.

[18] C. H. Choi, C. Baldizzone, J. P. Grote, A. K. Schuppert, F. Jaouen, K. J. Mayrhofer, *Angew. Chem. Int. Ed.* **2015**, *54*, 12753–12757.

[19] G. Zhang, R. Chenitz, M. Lefèvre, S. Sun, J.-P. Dodelet, *Nano Energy* **2016**, *29*, 111–125.

[20] J.-Y. Choi, L. Yang, T. Kishimoto, X. Fu, S. Ye, Z. Chen, D. Banham, *Energy Environ. Sci.* **2017**, *10*, 296–305.

[21] D. Banham, T. Kishimoto, Y. Zhou, T. Sato, K. Bai, J. I. Ozaki, Y. Imashiro, S. Ye, *Sci. Adv.* **2018**, *4*, eaar7180.

[22] C. H. Choi, H. K. Lim, M. W. Chung, G. Chon, N. R. Sahraie, A. Altin, M. T. Sougrati, L. Stievano, H. S. Oh, E. S. Park, F. Luo, P. Strasser, G. Drazic, K. J. J. Mayrhofer, H. Kim, F. Jaouen, *Energy Environ. Sci.* **2018**, *11*, 3176–3182.

[23] R. Chenitz, U. I. Kramm, M. Lefèvre, V. Glibin, G. Zhang, S. Sun, J.-P. Dodelet, *Energy Environ. Sci.* **2018**, *11*, 365–382.

[24] H. G. Zhang, H. T. Chung, D. A. Cullen, S. Wagner, U. I. Kramm, K. L. More, P. Zelenay, G. Wu, *Energy Environ. Sci.* **2019**, *12*, 2548–2558.

[25] K. Kumar, L. Dubau, M. Mermoux, J. Li, A. Zitolo, J. Nelayah, F. Jaouen, F. Maillard, *Angew. Chem. Int. Ed.* **2020**, *59*, 3235–3243.

[26] J. Weiss, H. G. Zhang, P. Zelenay, *J. Electroanal. Chem.* **2020**, *875*, 114696.

[27] X. H. Xie, C. He, B. Y. Li, Y. H. He, D. A. Cullen, E. C. Wegener, A. J. Kropf, U. Martinez, Y. W. Cheng, M. H. Engelhard, M. E. Bowden, M. Song, T. Lemmon, X. S. Li, Z. M. Nie, J. Liu, D. J. Myers, P. Zelenay, G. F. Wang, G. Wu, V. Ramani, Y. Y. Shao, *Nat. Catal.* **2020**, *3*, 1044–1054.

[28] M. Ferrandon, A. J. Kropf, D. J. Myers, K. Artyushkova, U. Kramm, P. Bogdanoff, G. Wu, C. M. Johnston, P. Zelenay, *J. Phys. Chem. C* **2012**, *116*, 16001–16013.

[29] U. I. Kramm, J. Herranz, N. Larouche, T. M. Arruda, M. Lefevre, F. Jaouen, P. Bogdanoff, S. Fiechter, I. Abs-Wurmbach, S. Mukerjee, J. P. Dodelet, *Phys. Chem. Chem. Phys.* **2012**, *14*, 11673–11688.

[30] Q. Jia, E. Liu, L. Jiao, S. Pann, S. Mukerjee, *Adv. Mater.* **2019**, *31*, e1805157.

[31] I. T. Bae, D. A. Tryk, D. A. Scherson, *J. Phys. Chem. B* **1998**, *102*, 4114–4117.

[32] U. Tylus, Q. Jia, K. Strickland, N. Ramaswamy, A. Serov, P. Atanassov, S. Mukerjee, *J. Phys. Chem. C* **2014**, *118*, 8999–9008.

[33] J. K. Li, S. Ghoshal, W. T. Liang, M. T. Sougrati, F. Jaouen, B. Halevi, S. McKinney, G. McCool, C. R. Ma, X. X. Yuan, Z. F. Ma, S. Mukerjee, Q. Y. Jia, *Energy Environ. Sci.* **2016**, *9*, 2418–2432.

[34] J. H. Zagal, I. Ponce, D. Baez, R. Venegas, J. Pavez, M. Paez, M. Gulppi, *Electrochem. Solid-State Lett.* **2012**, *15*, B90–B92.

[35] L. Osmieri, R. K. Ahluwalia, X. H. Wang, H. T. Chung, X. Yin, A. J. Kropf, A. E. Y. Park, D. A. Cullen, K. L. More, P. Zelenay, D. J. Myers, K. C. Neyerlin, *Appl. Catal. B* **2019**, *257*, 117929.

[36] N. Ramaswamy, U. Tylus, Q. Jia, S. Mukerjee, *J. Am. Chem. Soc.* **2013**, *135*, 15443–15449.

[37] Q. Jia, N. Ramaswamy, H. Hafiz, U. Tylus, K. Strickland, G. Wu, B. Barbiellini, A. Bansil, E. F. Holby, P. Zelenay, S. Mukerjee, *ACS Nano* **2015**, *9*, 12496–12505.

[38] J. Li, A. Alsudairi, Z. F. Ma, S. Mukerjee, Q. Jia, *J. Am. Chem. Soc.* **2017**, *139*, 1384–1387.

[39] M. Ferrandon, X. Wang, A. J. Kropf, D. J. Myers, G. Wu, C. M. Johnston, P. Zelenay, *Electrochim. Acta* **2013**, *110*, 282–291.

[40] P. Madkikar, D. Menga, G. S. Harzer, T. Mittermeier, A. Siebel, F. E. Wagner, M. Merz, S. Schuppler, P. Nagel, A. B. Muñoz-García, M. Pavone, H. A. Gasteiger, M. Piana, *J. Electrochem. Soc.* **2019**, *166*, F3032–F3043.

[41] T. Mittermeier, P. Madkikar, X. Wang, H. A. Gasteiger, M. Piana, *J. Electrochem. Soc.* **2016**, *163*, F1543–F1552.

[42] S. Ould-Chikh, I. Vollmer, A. Aguilar Tapia; **2018**; SSHADE/FAME; OSUG Data Center; Dataset/Spectral Data; https://doi.org/10.26302/SSHADE/EXPERIMENT_SOC_20181115_004.

[43] P. Li, I. W. Chen, J. E. Penner-Hahn, *J. Am. Ceram. Soc.* **1994**, *77*, 118–128.

[44] M. Wilke, F. Farges, P.-E. Petit, G. E. Brown, F. Martin, *Am. Mineral.* **2001**, *86*, 714–730.

[45] A. Zitolo, V. Goellner, V. Armel, M. T. Sougrati, T. Mineva, L. Stievano, E. Fonda, F. Jaouen, *Nat. Mater.* **2015**, *14*, 937–942.

[46] H. L. Fei, J. C. Dong, Y. X. Feng, C. S. Allen, C. Z. Wan, B. Volosskiy, M. F. Li, Z. P. Zhao, Y. L. Wang, H. T. Sun, P. F. An, W. X. Chen, Z. Y. Guo, C. Lee, D. L. Chen, I. Shakir, M. J. Liu, T. D. Hu, Y. D. Li, A. I. Kirkland, X. F. Duan, Y. Huang, *Nat. Catal.* **2018**, *1*, 63–72.

[47] D. Menga, J. L. Low, Y. S. Li, I. Arcon, B. Koyuturk, F. Wagner, F. Ruiz-Zepeda, M. Gaberscek, B. Paulus, T. P. Fellinger, *J. Am. Chem. Soc.* **2021**, *143*, 18010–18019.

[48] D. Menga, A. G. Buzanich, F. Wagner, T. P. Fellinger, *Angew. Chem. Int. Ed.* **2022**, *61*, e202207089.

[49] P. Madkikar, X. Wang, T. Mittermeier, A. H. A. Monteverde Videla, C. Denk, S. Specchia, H. A. Gasteiger, M. Piana, *J. Nanostruct. Chem.* **2017**, *7*, 133–147.

[50] P. Madkikar, T. Mittermeier, H. A. Gasteiger, M. Piana, *J. Electrochem. Soc.* **2017**, *164*, F831–F833.

[51] S. Meini, M. Piana, H. Beyer, J. Schwaemmlein, H. A. Gasteiger, *J. Electrochem. Soc.* **2012**, *159*, A2135–A2142.

[52] N. D. Leonard, K. Artyushkova, B. Halevi, A. Serov, P. Atanassov, S. C. Barton, *J. Electrochem. Soc.* **2015**, *162*, F1253–F1261.

[53] G. S. Harzer, J. N. Schwammlein, A. M. Damjanovic, S. Ghosh, H. A. Gasteiger, *J. Electrochem. Soc.* **2018**, *165*, F3118–F3131.

[54] A. M. Damjanovic, B. Koyuturk, Y. S. Li, D. Menga, C. Eickes, H. A. El-Sayed, H. A. Gasteiger, T. P. Fellinger, M. Piana, *J. Electrochem. Soc.* **2021**, *168*, 114518.

[55] A. Siebel, Y. Gorlin, J. Durst, O. Proux, F. Hasche, M. Tromp, H. A. Gasteiger, *ACS Catal.* **2016**, *6*, 7326–7334.

[56] B. Ravel, M. Newville, *J. Synchrotron Radiat.* **2005**, *12*, 537–541.